

# COHESIVE ZONE MODELING OF FAILURE IN UNDERFILLED BGA-PCB ASSEMBLIES UNDER BENDING

Saeed Akbari, Amir Nourani, Jan K. Spelt  
Department of Mechanical and Industrial Engineering  
University of Toronto  
Toronto, ON, Canada  
spelt@mie.utoronto.ca

## ABSTRACT

A cohesive zone model (CZM) was developed to simulate the delamination behavior of multilayer printed circuit boards (PCBs) assembled with ball grid array (BGA) components that were reinforced with an underfill epoxy adhesive. Two different delamination modes were observed in the bending specimens: delamination at the interface between the solder mask and the first conducting layer of the PCB, and PCB subsurface delamination at the interface between the epoxy and glass fibers of one of the prepreg layers. The cohesive parameters for each of the two delamination interfaces were determined from fracture tests of bending test specimens consisting of PCB substrates bonded with the underfill adhesive. The model was able to accurately predict the fracture load and failure mode of the underfilled BGA-PCB assemblies.

Key words: multilayer PCB, cohesive zone modeling, delamination, finite element analysis (FEA), underfill adhesive

## INTRODUCTION

Multilayer PCBs consist of conducting copper layers and woven glass-fiber epoxy insulating layers bonded together under heat and pressure. The copper layers are etched to create the required pattern of conducting traces, and the epoxy of the adjacent insulating layers fills the gaps where the copper was etched away, thereby generating copper-epoxy composite conducting layers [1]. An underfill adhesive is commonly used to fill the gap between the BGA and the PCB, and reinforce the solder balls in between. The underfilling creates new sites of potential delamination.

One of the main failure modes in PCB composite laminates is interlaminar damage or delamination during the soldering process, installation, service and repair [2-3]. It is therefore critical to understand the delamination mechanism and quantify the relevant properties governing the delamination. Delamination initiation and propagation in composite laminates is typically simulated using cohesive zone models (CZMs) [4-5]. In order to determine the cohesive law parameters, load-displacement data of fracture test of double cantilever beam (DCB) specimens are frequently used [6-7]. Fuchs and Fellner [8] used a CZM coupled with a finite element model (FEM) to simulate the delamination of mode I DCB specimens made of 0.65, 2, and 5 mm thick PCB adherends. The fracture specimens consisted of laminated

woven glass-fiber prepregs with a Teflon film to form a 20 mm pre-crack. The 5 mm thick DCBs were used to determine the cohesive parameters, and the model was validated by comparing the predicted and measured fracture loads for the other mode-I DCBs. The simulation results showed a reasonable agreement with the experimental data. However, the proposed model was not used for delamination prediction in PCBs assembled with microelectronic components.

It should be noted that multilayer PCBs are not homogeneous through their thickness, because they consist of conducting and insulating layers of different properties bonded at interfaces that may have different strengths as reflected by the critical strain energy release rate,  $G_c$ . In a previous study [9], the present authors tested underfilled BGA-PCB assemblies under bending loading conditions. The specimens always failed in the PCB, and the location of delamination interface in the multilayer PCBs changed with the size of the spew fillet of the underfill epoxy adhesive.

The main objective of the present work was to develop a CZM to predict the initiation and propagation of delamination in underfilled BGA-PCB assemblies tested under different bending conditions. Since delamination always initiated in the PCB, the traction-separation parameters of the CZM were obtained from fracture tests of bending specimens made from PCBs bonded with the underfill epoxy, without any microelectronic components. The two-parameter CZM was then coupled with finite element analysis (FEA) to simulate the delamination and progressive failure in the BGA-PCB assemblies.

## EXPERIMENTAL METHODS

### Board Assembly

Thin-profile fine-pitch ball grid array packages (iNAND Embedded Flash Drives, SanDisk, Milpitas, USA) were assembled on multilayer PCBs. Table 1 shows the distribution of the PCB layers. The package had a trilayer structure including a silicon chip interconnected to a bismaleimide-triazine (BT) substrate, and encapsulated in an epoxy molding compound (EMC).

The solder reflow process was performed using a surface mount technology (SMT) development line (Cambridge, BlackBerry, Canada). The SMT line included production equipment for solder paste screen printing, package

placement, and reflow soldering. After reflow, the diameter, height and pitch of the solder balls connecting the BGAs to the PCB were 300  $\mu\text{m}$ , 200  $\mu\text{m}$ , and 500  $\mu\text{m}$ , respectively. After solder reflow, underfilling was conducted to reinforced the solder balls. A heat-cure low-viscosity adhesives was selected for underfilling (properties of Table 2). In most cases, an automated dispenser was used to underfill the BGA-PCB assemblies. It applied a specific volume of underfill to the edge of each BGA package where it flowed under the BGA, and filled the gap between the BGA and the PCB as well as between the solder balls. The properties of the BGA-PCB assembly are given in Table 2.

**Table 1.** PCB layout (symmetric about layer 9, total number of layers=17). SM=solder mask, PL=plated copper, RCC=resin coated copper, PR=prepreg [9].

Layer No.	1	2	3	4	5	6	7	8	9
Material	SM	PL	RCC	PL	PR	PL	PR	PL	PR
Thickness ( $\mu\text{m}$ )	20	28	50	28	50	28	19	17	200

**Table 2.** Properties of the BGA-PCB assembly [9-10].

Material	Thickness ( $\mu\text{m}$ )	Young's modulus (GPa)	Poisson's ratio
BT substrate	170	14.5	0.11
Silicon die	320	130	0.28
EMC	680	16.7	0.25
Solder	200	51	0.4
PCB	1,000	$E_x = E_y = 21.8$ $E_z = 3.5$	$\nu_{xz} = \nu_{yz} = 0.1$ $\nu_{yz} = 0.25$
Underfill	200	2.6	0.35

A spew fillet was created during the underfilling process at the edge of each BGA package (Fig. 1a). The size of this as-manufactured underfill fillet depended on the underfill viscosity and the surface tension of the underfill and the adjoining surfaces. The fracture tests of the BGA-PCB assemblies conducted in [9] showed that the strength is proportional to the underfill fillet size. In order to enlarge the fillet size (Fig. 1b), in a number of BGA-PCB DCB specimens, extra underfill was dispensed and cured on the PCB surface close to the as-manufactured fillet. In the present work, the effect of the fillet size was studied using the bending specimens described in the following section.

ASTM D3039 was used to measure the in-plane tensile modulus and tensile strength of the PCB in [9] as 21.8 GPa and 254 MPa, respectively. The PCB tensile behavior was linear until fracture, because the PCB mostly consisted of relatively brittle glass fibers and epoxy resin. The out-of-plane ( $z$  direction) tensile properties of the PCB presented in Table 2 were obtained from ref. [10].

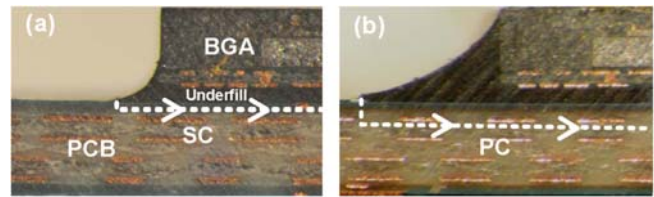


**Figure 1.** Cross-sections of underfilled BGA-PCB assemblies revealing the different spew fillets of the underfill epoxy adhesive. a) as-manufactured fillet, b) reinforced fillet.

### Test Vehicles

Fracture specimens were prepared from the BGA-PCB assemblies and were tested in the bending configurations of Fig. 2. A diamond saw blade was used to cut the BGA-PCB assemblies along the dashed lines shown in Fig. 3b. The free surface of the BGA was sanded using a 400-grit sand paper, cleaned with acetone, and then was bonded to a rigid support. The specimen of Fig. 2 was made with an as-manufactured and a large fillet as described in Fig. 1. It was tested at a constant loading rate of 1.5 mm/min, and the applied force was measured using a 200 N load cell.

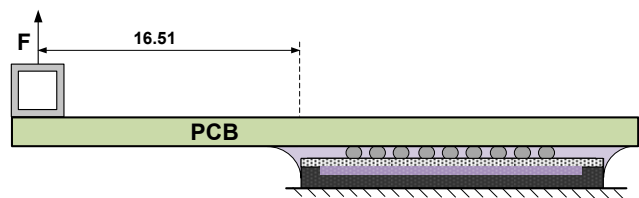


**Figure 2.** Underfilled BGA-PCB bending test specimen.

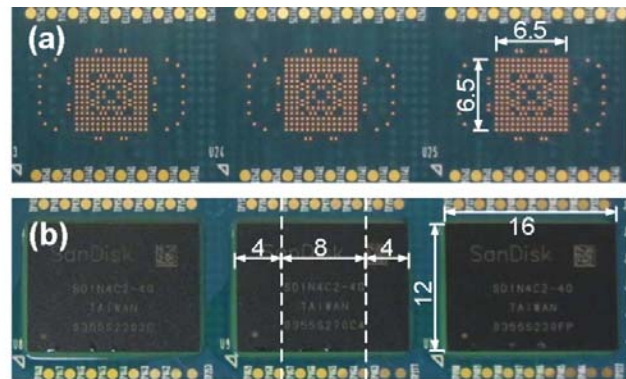


**Figure 3.** a) PCB surface with copper pads before package assembly. b) BGA packages mounted on PCB. The test specimens were prepared by cutting the BGA-PCB assembly along dashed lines. Dimensions in mm [9].

### Determination of cohesive parameters for PCB delamination

Two distinct failure modes were seen in the bending configuration of Fig. 2, similar to those observed within DCB specimens of ref. [9]. The first failure mode involved crack growth at the interface between the solder mask (layer 1 in Table 1) and the first conducting layer (layer 2). This failure mode was named SC (solder mask cracking) in ref. [9]. In the second failure mode a crack propagated at the

interface between the glass fibers and epoxy of one of the prepreg layers (layer 7). This failure mode was called PC (PCB cracking) [9]. Further details of these failure modes are given in the following sections.

The quasi-static, mode I interlaminar strain energy release rate,  $G_{nc}$ , for both failure SC and PC modes were measured in [11] using quasi-static fracture tests of the PCB-UF-PCB DCB specimens of Fig. 4. The thickness of the underfill adhesive layer was 127  $\mu\text{m}$  controlled using steel wires. The DCB failure mode was always SC when the solder mask was present on the PCB surface, and PC when the solder mask layer was sanded away from the PCB surface using a 400 grit sand paper. In this work, the quasi-static cohesive strengths for both the SC and PC failure modes were obtained by comparing the experimental load-displacement data from these DCB tests of [11] (Fig. 4) with the CZM simulation results. This process is explained in greater detail in the following sections. These cohesive strengths and the  $G_{nc}$  values from [11] were then used in the quasi-static CZM described in the next section to simulate the fracture of the bending BGA-PCB specimens of Fig. 2.

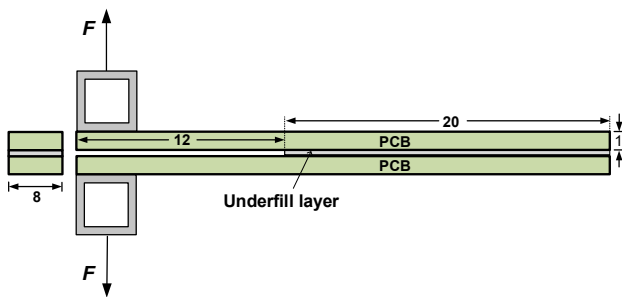


**Figure 4.** DCB specimen tested in [11] to determine quasi-static  $G_{nc}$  for both SC and PC failure modes. Dimensions in mm. Not to scale.

## EXPERIMENTAL RESULTS

### Failure modes and cracking sequence

The underfilled BGA-PCB assemblies of Fig. 2 always failed in the PCB, and in no case did the underfill layer itself crack, because the average  $G_{nc}$  for the SC and PC failure modes, based on the fracture tests conducted in [11] using the PCB-UF-PCB DCB specimens of Fig. 4, was 180 and 230  $\text{J/m}^2$ , respectively. This was significantly lower than the quasi-static  $G_{nc}$  for the cohesive failure of the underfill, measured using aluminum-UF-aluminum DCB fracture specimens.

Two different failure modes were observed (Fig. 5) in the BGA-PCB specimens. Depending on the underfill fillet size, the crack propagated either at the interface between layer 1 (epoxy solder mask) and the epoxy of layer 2 of the PCB (Table 1) [11], referred to as solder mask cracking (SC), or within the layer 7, referred to as PCB cracking (PC).

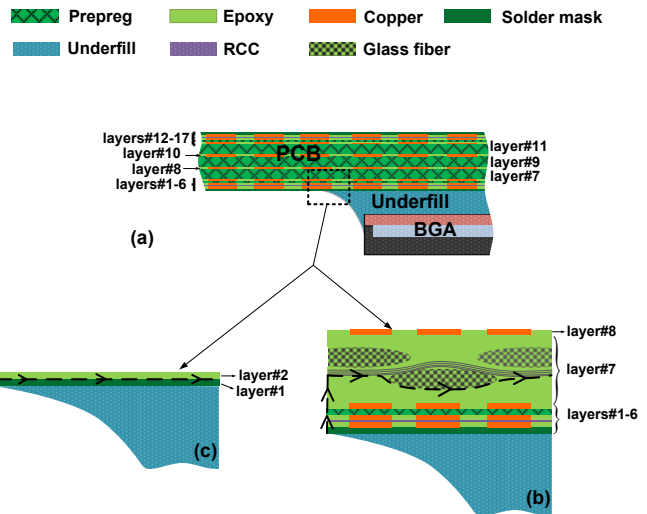


**Figure 5.** Different failure modes observed in PCB of BGA-PCB assemblies. a) Cross-section of a BGA-PCB DCB specimen, b) PCB cracking (PC), c) solder mask cracking (SC) [9].

Fig. 6 shows the cracking sequence of the PCB, which involves two competing failure mechanisms: delamination at either the SC or PC interfaces, which was simulated based on a CZM in the next section, and the subsequent rupture of the PCB cracked layer, also modeled according to the maximum stress criterion in the next section.

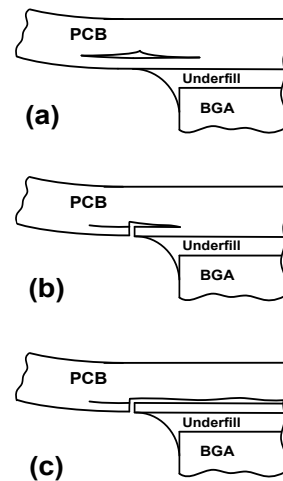


**Figure 6.** Cracking sequence in the multilayer PCB in order of occurrence: a) delamination initiation in horizontal direction at either PCB layer 7 (PC failure mode) or at the interface between layers 1 and 2 (SM failure mode), b) PCB rupture in vertical direction due to tensile stresses, c) delamination propagation in horizontal direction [9].

The failure started as a delamination at an interface in layer 7 (PC failure mode) or between layers 1 and 2 (SC failure mode) (Fig. 6a), because the out-of-plane tensile strength of the PCB was much lower than its in-plane tensile strength. After delamination initiation in either the PC or SC modes, stress became concentrated in the PCB delaminated layer

until it exceeded the ligament tensile strength (Fig. 6b). Finally, the original delamination propagated to the end of the PCB (Fig. 6c).

It should be noted that the thickness of the cracked (delaminated) layer (Fig. 6a) was quite different in the SC and PC failure modes (25  $\mu\text{m}$  in SC and 250  $\mu\text{m}$  in PC, as reported in [11]).

### Load displacement data

Figure 7 shows a representative experimental load-displacement curve for the PCB-UF-PCB DCB specimens (Fig. 4) for both the SC and PC failure modes under quasi-static loading. The maximum load corresponded to delamination initiation (Fig. 6a) and the rupture of the delaminated layer (Fig. 6b), which occurred simultaneously. The curve was almost linear until fracture, showing that the PCB had little or no plastic deformation before damage initiation. The FEM predictions of the load-displacement data are also presented in Fig. 7. These will be discussed in the following sections.

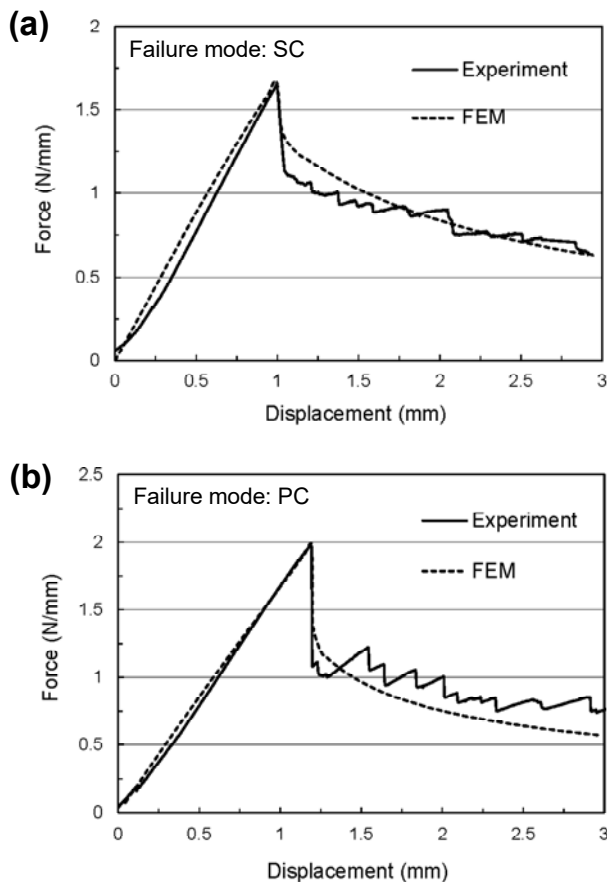


**Figure 7.** Comparison between the numerical (FEM) and experimental load-displacement curves for representative DCB joints of Fig. 4: a) SC failure mode, b) PC failure mode.

### FINITE ELEMENT ANALYSIS

In order to model the BGA-PCB specimen (Fig. 2) or PCB DCB calibration specimen (Fig. 4), a 2D isotropic linear

elastic finite element model (FEM) with 4-node plane-strain structural elements (Plane 182, ANSYS®15, Ansys Inc, Canonsburg, PA) was used (Fig. 8). The boundary conditions considered in the FEM were consistent with the fixation of the DCB and bending specimens (Figs. 2 and 4). The element size was changed smoothly from 25  $\mu\text{m}$  in the vicinity of the cohesive interface to 100  $\mu\text{m}$  in the substrates. A convergence study showed that the results were independent of the element size over this range.

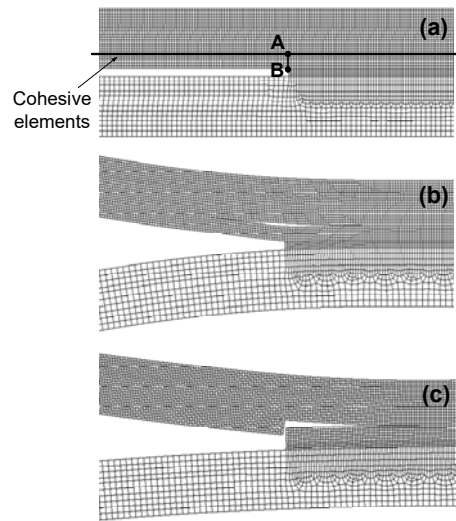


**Figure 8.** Finite element mesh of the specimen of Fig. 4 near the crack initiation point for the PC failure mode, a) before load application, b) delamination initiation, c) rupture of the PCB cracked layer and delamination growth.

### PCB delamination: Cohesive zone modeling

The finite element model was used to simulate the delamination initiation and propagation in the PCB. In order to maintain the equilibrium of the shear and tensile stresses, a mixed-mode CZM was used. However, only the mode I CZM governed delamination response.

A bilinear traction-separation law (Fig. 9) was used for delamination analysis, in which it is assumed that with increasing load the cohesive stress linearly increases to a maximum value ( $\sigma_{nc}$ ). After the maximum point, softening and damage initiates at the interface. As the damage develops, the cohesive stress decreases until separation reaches a critical value ( $\sigma_{nc}$ ) where cohesive stress vanishes and delamination initiation takes place with the elements bounding the interface separating completely. The area under the traction separation curve is equal to the fracture energy, or critical strain-energy release rate,  $G_{nc}$ , as measured using the DCB specimen of Fig. 4.

Surface-to-surface contact elements were used to model both the SC and PC interfaces. To this end, the contact surface on one side of the cohesive interface was defined with the 3-node CONTA172 elements, while the target

surface on the other side was defined with TARGE169 elements.

The default stiffness in ANSYS ( $K_n = 10^{14}$  N/m<sup>3</sup>) was used. An iterative procedure was used to find the cohesive strength,  $\sigma_{nc}$ , that provided the best match between the simulation predictions in the calibration PCB specimen (Fig. 4) and the experimental load–displacement data.

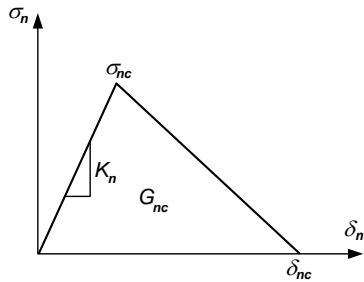


**Figure 9.** The bilinear traction–separation law used to model PCB delamination in the FEM.

**PCB rupture: maximum stress criterion**

To model damage initiation and propagation in the FEM, the applied load was incrementally increased until delamination initiated in the PCB along the designated cohesive interface shown in Figs. 6a and 8b. As illustrated in Fig. 6b, after some delamination in the horizontal direction, the axial stress due to bending in the cracked PCB layer was large enough to give rise to PCB rupture along the path A-B in Fig. 8a. This second failure mechanism had to be modeled in the FEM. Otherwise the predicted load behavior was incorrect, with the load dropping slightly after delamination initiation, and then increasing again continuously, because the PCB cracked layer continued to carry the load as the delamination propagated.

In order to precisely predict the experimental load displacement curve, the rupture of the PCB cracked layer along path A-B was modeled by joining nodes on the two sides of the path A-B with a constraint relation. When the PCB tensile strength was reached, all constrained nodes were released to simulate the PCB rupture along A-B. As a result, the load dropped (Fig. 7), and the second phase of delamination began (Figs. 6c and 8c).

**CZM calibration**

Figure 7 compares the experimental data for the quasi-static fracture test of the PCB-UF-PCB DCB specimens (Fig. 4) with the simulation results for both the SC and PC failure modes. The cohesive strength,  $\sigma_{nc}$ , was adjusted for each failure mode so that the peak load in the FEM was equal to that of the experimental curve. Figure 7 shows that the finite element model described in the previous sections was able to predict the experimental load displacement curve. The cohesive parameters of the SC and PC interfaces are presented in Table 3.

**Table 3.** CZM parameters for the PC and SC failure modes.

Failure mode	$K_n$ (N/m <sup>3</sup> )	$\sigma_{nc}$ (MPa)	$G_{nc}$ (J/m <sup>2</sup> )
PC	$10^{14}$	4.8	230
SC	$10^{14}$	16.1	180

**COMPARISON OF FEM PREDICTIONS AND EXPERIMENTAL MEASUREMENTS**

This section discusses the ability of the proposed model to predict the fracture loads and failure modes observed in the underfilled BGA-PCB bending specimen of Fig. 2 with two different fillet sizes (Fig. 1). Figure 10 compares the experimental load-displacement curves for small and large fillets with those predicted using the traction-separation relations of Table 3 in the finite element model described in the previous section. The model correctly predicted the SC failure mode with the small fillet and the PC mode for the large fillet (Fig. 1), as shown in Fig. 11. This change in the crack path with the fillet size was due to the higher stress concentration at the toe of the small underfill fillet, which caused the highest stresses to occur between layer 1 and 2 and so initiate the SC failure mode. Figure 10 also shows good agreement in the behavior to the maximum load and the subsequent unloading to the point where the crack arrested at the first row of solder balls. After this point, the experimental results of Fig. 10a show that the load increased again until crack extended to the next row of balls, sometimes through the solder and sometimes under it within the PCB [11]. Since only the crack initiation load (the maximum load) was of interest in this study, the crack arrest and subsequent propagation was not modeled.

The average fracture load for the large fillet was 1.7 times larger than the corresponding value for the small fillet. Five specimens were tested for each fillet size, with standard deviation of less than 10% for each fillet size.

In the simulation results for the small fillet, the peak load corresponded to the SC mode delamination initiation and the simultaneous rupture of the PCB. For the large fillet, the PC delamination initiation in the model was marked by a small nonlinearity in the rising slope of the load-displacement curve near the peak (Point A in Fig. 10b), which resulted from the abrupt change in the PCB stiffness after crack initiation. This nonlinearity was not observed in the experimental curve, probably because of the smooth transition from delamination initiation to the loading of the PCB ligament (line A-B in Fig. 8). The predicted load then increased after delamination initiation until the PCB tensile strength in the cracked layer was reached and the associated nodes (path A-B in Fig. 8) were released, thereby decreasing the load significantly.

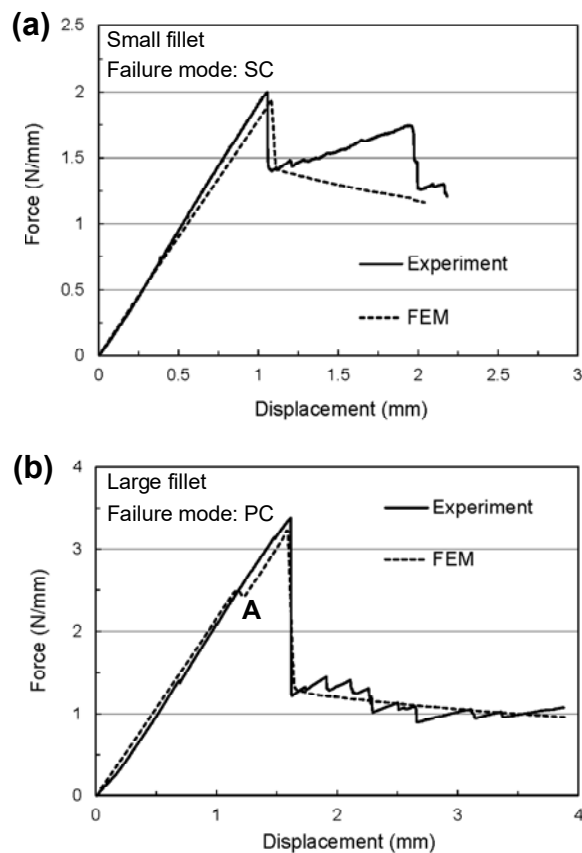


**Figure 10.** Representative curves of measured and predicted load per unit width as a function of displacement for BGA-PCB specimens of Fig. 3a with two different fillet sizes (Fig. 2): a) small fillet, b) large fillet.

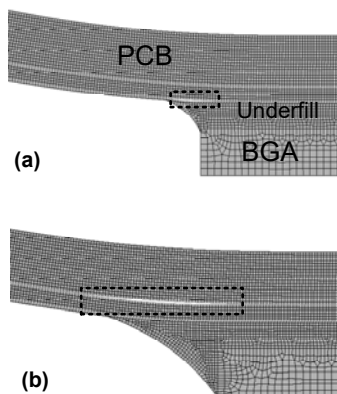


**Figure 11.** FEM predictions of the effect of the underfill fillet size on the location of the initial delamination initiation within the PCB. Delamination initiated at the SC interface for relatively small fillets, and at the PC interface for large fillets.

## CONCLUSIONS

Two different subsurface delamination modes, were observed in multilayer PCBs assembled with BGAs and tested under bending loading conditions. A CZM was presented to predict delamination initiation and propagation in these PCB-BGA assemblies. The cohesive parameters

were determined from fracture tests of DCB specimens consisting of PCB substrates bonded with the underfill adhesive. The model was then coupled with an FEM to predict the transitions in failure mechanisms and the bending strength of underfilled BGA-PCB specimens fabricated in an SMT line, and fracture tested under bending configurations.

The CZM could also successfully predict the change of the failure mode with underfill fillet size; i.e. near-surface delamination for relatively small fillets, and subsurface delamination for larger fillets. This was attributed to the lower stress concentration in PCB-fillet interface for larger fillets.

Overall, it was demonstrated that this model could accurately predict the fracture loads of these underfilled BGA-PCB assemblies. The model was also able to predict the correct crack path as it changed with fillet size.

## ACKNOWLEDGEMENTS

The work was financially supported by Blackberry and the Natural Sciences and Engineering Research Council of Canada.

## REFERENCES

- [1] Fuchs, P.F., Pinter, G. and Tonjec, M., 2012. Determination of the orthotropic material properties of individual layers of printed circuit boards. *Microelectronics Reliability*, 52(11), pp.2723-2730.
- [2] Sood, B., Sanapala, R., Das, D., Pecht, M., Huang, C.Y. and Tsai, M.Y., 2010. Comparison of Printed Circuit Board Property Variations in Response to Simulated Lead-Free Soldering. *IEEE Transactions on Electronics Packaging Manufacturing*, 33(2), pp.98-111.
- [3] Shi, H., Che, F. and Ueda, T., 2011. Experiment and numerical analysis for edge and corner bonded PoP bottom package assemblies under four-point bending. *Microelectronics Reliability*, 51(9), pp.1850-1855.
- [4] Giuliese, G., Palazzetti, R., Moroni, F., Zucchelli, A. and Pironi, A., 2015. Cohesive zone modelling of delamination response of a composite laminate with interleaved nylon 6, 6 nanofibres. *Composites Part B: Engineering*, 78, pp.384-392.
- [5] Manshadi, B.D., Farmand-Ashtiani, E., Botsis, J. and Vassilopoulos, A.P., 2014. An iterative analytical/experimental study of bridging in delamination of the double cantilever beam specimen. *Composites Part A: Applied Science and Manufacturing*, 61, pp.43-50.
- [6] Heidari-Rarani, M., Shokrieh, M.M. and Camanho, P.P., 2013. Finite element modeling of mode I delamination growth in laminated DCB specimens with R-curve effects. *Composites Part B: Engineering*, 45(1), pp.897-903.
- [7] Farmand-Ashtiani, E., Alanis, D., Cugnoni, J. and Botsis, J., 2015. Delamination in cross-ply laminates:

Identification of traction–separation relations and cohesive zone modeling. *Composites Science and Technology*, 119, pp.85-92.

- [8] Filipp Fuchs, P., Fellner, K. and Pinter, G., 2013. Local damage simulations of printed circuit boards based on in-plane cohesive zone parameters. *Circuit World*, 39(2), pp.60-66.
- [9] Akbari, S., Nourani, A. and Spelt, J.K., 2016. Effect of adhesive fillet geometry on bond strength between microelectronic components and composite circuit boards. *Composites Part A: Applied Science and Manufacturing*, 87, pp.228-236.
- [10] Meyyappan, K., McAllister, A., Kochanowski, M. and Hsu, I., 2008. Effects of glue on the bend performance of flip chip packages. *IEEE Transactions on Components and Packaging Technologies*, 31(3), pp.670-677.
- [11] Akbari, S., Nourani, A. and Spelt, J.K., 2016. Bending strength of adhesive joints in microelectronic components: Comparison of edge-bonding and underfilling. *Composites Part A: Applied Science and Manufacturing*, 88, pp.178-189.